This is a preprint, the final version is subject to change, of the American Mineralogist (MSA)
Cite as Authors (Year) Title. American Mineralogist, in press.
DOI: https://doi.org/10.2138/am-2020-7098

REVISION 2

PARTITION COEFFICIENTS OF TRACE ELEMENTS BETWEEN CARBONATES AND MELT AND SUPRASOLIDUS PHASE RELATION OF CA-MG-CARBONATES AT 6 GPA

Sieber Melanie J.[1*], Wilke Franziska [1], Koch-Müller Monika[1]

[1] GFZ German Research Centre for Geosciences, Section 3.6 and 3.1, Telegrafenberg, 14473 Potsdam, Germany

*corresponding author: E-mail address: sieber@gfz-potsdam.de

Abstract

The presence of Ca-Mg-carbonates affects the melting and phase relations of peridotites and eclogites in the mantle and (partial) melting of carbonates liberates carbon from the mantle to shallower depths. The onset and composition of incipient melting of carbonated peridotites and carbonated eclogites are influenced by the pure $CaCO_3$-$MgCO_3$-system making understanding of the phase relations of Ca-Mg-carbonates fundamental in assessing carbon fluxes in the mantle. By performing high pressure and temperature experiments, this study clarifies the suprasolidus phase relations of the nominally anhydrous $CaCO_3$-$MgCO_3$-system at 6 GPa showing that Ca-Mg-carbonates will (partially) melt for temperatures above ~1300 °C. A comparison with data from thermodynamic modelling confirms the experimental results. Furthermore, partition coefficients for Li, Na, K, Sr, Ba, Nb, Y and rare earth elements between calcite and dolomitic melt, Ca-magnesite and dolomitic melt and magnesite and dolomitic melt are established.

Experiments were performed at 6 GPa and between 1350 to 1600 °C utilizing a rotating multi-anvil press. Rotation of the multi-anvil press is indispensable to establish equilibrium between solids and carbonate liquid. Major and trace elements were quantified with EPMA and LA-ICP-MS, respectively.

The melting temperature and phase relations of Ca-Mg-carbonates depend on the Mg/Ca-ratio. For instance, Ca-rich carbonates with a molar Mg/(Mg+Ca)-ratio (X_{Mg}) of 0.2 will transform into a dolomitic melt (X_{Mg}=0.33-0.31) and calcite crystals (X_{Mg}=0.19-0.14) at 1350-1440 °C. Partial melting of Mg-rich carbonates (X_{Mg}=0.85) will produce a dolomitic melt (X_{Mg}=0.5-0.8) and Ca-bearing magnesite (X_{Mg}=0.89-0.96) at 1400-1600 °C. Trace element distribution into calcite and magnesite seems to follow lattice constraints for divalent cations. For instance, the compatibility of calcite (X_{Mg}=0.14-0.19) for Sr and Ba decreases as the cation radii increases. Ca-Mg-carbonates are incompatible for rare earth elements (REEs), whereby the distribution between carbonates and dolomitic melt depends on the Mg/Ca ratio and temperature. For instance, at 1600 °C, partition coefficients between magnesite (X_{Mg}=0.96) and dolomitic melt (X_{Mg}=0.8) vary by two orders of magnitudes from 0.001 to 0.1 for light-REEs to heavy-REEs. In contrast, partition coefficients of REEs (and Sr, Ba, Nb and Y) between magnesite (X_{Mg}=0.89) and dolomitic melt (X_{Mg}=0.5) are more uniform scattering marginal between ~0.1-0.2 at 1400 °C.

Keywords

Melt relations of carbonates at 6 GPa (~200 km)

Deep carbon cycle

Trace element partitioning

Carbonate stability in the mantle

Introduction

Ca-Mg-carbonates ($(Ca,Mg)CO_3$) are introduced into the mantle at subduction zones, while volcanic eruption outgases carbon back to the lithosphere and atmosphere (Hazen et al. 2013). Within the subducting slab, carbonates are most abundant in sediments and in the

hydrothermally altered parts of the oceanic crust (Alt and Teagle 1999). During heating and compression, some carbon is released from the subducting lithologies by decomposition and devolatilisation into a mobile phase (fluid or melt). Carbonic fluids eventually return to the surface via arc related magmatism and by diffuse outgassing (Hazen et al. 2013; Kelemen and Manning 2015) or may interact with (hydrated) peridotites in the subducting slab and with the supra-subduction mantle to form Ca-Mg-carbonates (Piccoli et al. 2016; Scambelluri et al. 2016; Sieber et al. 2018). However, in the absence of water, carbonates are stable along typical subduction zone geotherms. Therefore, carbonate bearing lithologies in the slab that do not experience pervasive dehydration or fluid infiltration can transport carbonates to greater mantle depths (Gorman et al. 2006; Kerrick and Connolly 1998; Kerrick and Connolly 2001). The presence of some carbonates in the mantle is evidenced, for instance, by carbonate-bearing ultra-high pressure metamorphic rocks (Korsakov and Hermann 2006; Shatsky et al. 2006), carbonate-bearing mantle xenoliths (Ionov et al. 1993; Ionov et al. 1996) and inclusions in diamonds (Stachel and Harris 2008; Wang et al. 1996).

Experimental studies demonstrate the stability of carbonates at the solidus of carbonated peridotites and eclogites and flag the relevance of carbonates to their melt relations and melting temperature (Brey et al. 2008; Dasgupta et al. 2004; Yaxley and Green 1994). For instance, the mantle solidus is reduced from ~1730 °C to ~1250-1380 °C at 6 GPa in the presence of carbonates (Dalton and Presnall 1998; Dasgupta and Hirschmann 2010; Hirschmann 2000). Even small amounts of carbonates can incite melting of peridotites, whereby carbonates are completely consumed to form dolomitic melts according to the approximate reaction of $2MgCO_3$ (magnesite) + $CaMgSi_2O_6$ (clinopyroxene) = $CaMg(CO_3)_2$ (liquid) + $Mg_2Si_2O_6$ (orthopyroxene) (Dalton and Presnall 1998). Low-degree melting of a carbonated mantle produces CO_2-rich melts which are potentially the precursor of carbonatites and kimberlites (Dalton and Wood 1993; Kruk et al. 2018; Yaxley and Brey

2004). The presence of CO_2-rich melts may contribute to the low electrical conductivity of the asthenosphere (Gaillard et al. 2008).

The composition of the incipient melt from partial melting of carbonated peridotites and carbonated eclogites is influenced by the melt relations of the pure $CaCO_3$-$MgCO_3$-system (Dalton and Presnall 1998; Dasgupta and Hirschmann 2006; Yaxley and Brey 2004). Thus, the melting point and suprasolidus phase relations of carbonates are fundamental in assessing carbon fluxes in the mantle. Despite the mentioned relevance of Ca-Mg-carbonates, their liquidus and suprasolidus phase relations remain controversial. Comparison of recent experimental studies reveals an offset of ~100-200 °C for the nominally anhydrous liquidus at 6 GPa (Buob et al. 2006; Müller et al. 2017; Shatskiy et al. 2018). This discrepancy is critical for the onset and degree of melting. For instance, at 6 GPa and between ~1300 and 1400 °C carbonates will either melt over a wide compositional range of $Ca_{0.1\text{-}0.9}Mg_{0.9\text{-}0.1}CO_3$ (Müller et al. 2017) or will be stable (Shatskiy et al. 2018). By performing high pressure and temperature experiments, this study clarifies the suprasolidus phase relations of Ca-Mg-carbonates at 6 GPa and compares the results to thermodynamic modelling of the $CaCO_3$-$MgCO_3$-system and to previous experimental studies.

Carbonate-rich melts are superb metasomatic agents, because they are buoyant with respect to peridotites, show high solubility for other volatiles (e.g. H_2O) and can be enriched in trace elements (Dalton and Wood 1993; Keppler 2003). Since the incipient melts of carbonated peridotites and carbonated eclogites are influenced by the pure carbonate-system, the trace element signature of near solidus, CO_2-rich liquids might also be influenced by the distribution of trace elements between carbonates and CO_2-rich melts. Thus, this study provides, for the first time, partition coefficients of Li, Na, K, Sr, Ba, Nb, Y and rare earth elements between calcite and dolomitic melt and magnesite and dolomitic melt at 6 GPa.

This is a preprint, the final version is subject to change, of the American Mineralogist (MSA)
Cite as Authors (Year) Title. American Mineralogist, in press.
DOI: https://doi.org/10.2138/am-2020-7098

Experimental methods

Two starting mixtures containing natural magnesite ($Mg_{29.6}Fe_{0.2}Mn_{0.1}Ca_{0.1}(CO_3)_{10}$ from Brumado, Brazil) and synthetic $CaCO_3$ regulating $X_{Mg} = \frac{n_{MgCO_3}[mol]}{n_{MgCO_3}[mol] + n_{CaCO_3}[mol]}$ to 0.85 (CM1) and 0.2 (CM2) were used in multi-anvil experiments (Table 1). Starting mixtures (CM1 and CM2) were doped with laboratory grade Li-, Na-, K-, Ba- and Sr-carbonate and Pb-, Nb- Y-oxides and rare earth elements (REEs) as oxides (purities ≥99.9 %; expect for La_2O_3 with a purity of 94%). All starting mixtures were ground in acetone for ~0.5 h and dried at ~120 °C for >48 h before loading into cold-sealed Pt-capsules. Pt-capsules had an outer height and diameter of 3 mm and 2 mm, respectively, and a wall thickness of 0.2 mm. An 18/11-assembly and a stepped graphite heater, minimizing the temperature (T) gradient across the capsule (Walter et al. 1995), were employed. Assembled octahedrons were stored at ~120 °C until conducting the experiment. Using the same assembly and multi-anvil apparatus, the absence of a T-gradient and a T-accuracy within 1% at 1500 °C was verified previously by applying the two-pyroxene geothermometer (Müller et al. 2017). Temperature was monitored over the run duration of 6 h with a Type C thermocouple (WRe5%-WRe26%-wires) surrounded by BN-powder to establish reduced conditions preventing a temporal drift of the measured temperature (Watenphul et al. 2009). The thermocouple failed in run A and temperature was controlled by the heating power. Experiments were conducted at 6 GPa, between 1350 to 1600 °C for 6 h in a Walker style multi-anvil apparatus. To encourage equilibrium between melt and crystals, the press was continuously rotated by 180° around its axis with 5°/sec and rotation was started before heating. The steady rotation was stopped to separate melt and crystals within ≲30 sec before quenching.

Methods

Analytical Methods

After the multi-anvil experiments, the recovered capsules were mounted, polished and C-coated for Electron Probe Micro Analyzes (EPMA). Quantitative wavelength dispersive spectrometry (WDS) was performed on a JEOL Superprobe JXA-8230 and a JEOL Hyperprobe JXA-8500F. For accurate quantification of Mg, Ca, Fe, Mn, Ba and Sr in carbonates, an acceleration voltage of 15 kV, a beam current of 1-10 nA, a probe size of 5-40 µm and relative short measurement times between 30 to 70 sec (for background and peak) were applied. Those analytical parameters are reported as optimal for precise electron probe micro-analyzes of carbonates (Zhang et al. 2017). To analyze melt-pockets in run D (Figure 1d, h), the size of the electron beam needed to be reduced to 1 µm. PRZ-matrix correction was applied and various carbonate standards were analyzed during the course of the analytical sessions to ensure the quality of measured data.

Afterwards, the trace element composition was determined by LA-ICP-MS (Laser Ablation - Inductively Coupled Plasma - Mass Spectrometry) using a Geolas Compex Pro 193 nm excimer laser coupled to a Thermo iCAP triple quad ICP-MS. The laser was operated with a frequency of 10 Hz and energy of 140 mNm. The diameter of the round laser spot ranged between 16 to 44 µm. Analyzes took place near the EPMA positions and Ca was used as reference element for quantification. NIST 610 was selected as the calibration standard and NIST 612 and Macs3 Ca-carbonate served as secondary standards for quality control. Reference values were taken from Jochum et al. (2011) and http://georem.mpch-mainz.gwdg.de. For data processing, the software Iolite was applied.

Raman measurements were performed to confirm the absence of hydrous phases using a HORIBA Jobin Yvon LabRAM HR800 VIS spectrometer with a DPSS laser of 405 and

473 nm wavelength. The spectral ranges were 100-1200 cm^{-1} and 3000-4000 cm^{-1} and the data acquisition time ranged from 10 to 30 sec.

Phase proportions and thermodynamic model

To calculate the mass proportions of solid carbonates and carbonate melts for each experiment, first the volume of carbonates and melt was obtained from geometrical constraints and then the density of solid carbonates was computed for conversion into mass%. In run A and B the volume of the melt was calculated from averaging the area of the semicircles in which the melt occurs (Figure 1a, b) and assuming the semicircle continues around the whole, inner capsule wall. Solid carbonates fill then the rest of the total, inner capsule volume. For simplification, the capsule volume prior to the experiment was used. Consequently, the obtained proportions of melts are slightly underestimated and the proportions of solid carbonates are somewhat overestimated. To obtain the volume of carbonate crystals in run C, we assumed the solid fraction occurs in a half-ball at the top of the capsule and in a half-ball plus cylinder at the bottom of the capsule. For run D, the software ImageJ was used to compute the area proportion of melt and solids from the contrast difference in BSE-images.

For conversion into mass proportions (listed in Table 1), the total weight of the system and the density of solid carbonates were needed. The latter was computed at run PT-conditions with Perple_X (Connolly 2005) using the Holland and Powell (1998) data base as revised by the authors in 2002. In the calculations the solid solution model for carbonates after Franzolin et al. (2011) was applied. The calibration of this solid solution bases upon subsolidus piston-cylinder experiments performed in the $CaCO_3$-$MgCO_3$-$FeCO_3$ system at 3.5 GPa and 900-1100 °C.

The error on the calculated phase proportions was not quantified, but uncertainties in the geometrical obtained volume proportions (e.g. the inner volume of the capsule prior to the

experiment), the computed densities (extrapolation from data based on experiment at lower PT) and measured compositions may contribute to the error.

Results

Textures and phase assemblages

In all experiments, a solid and liquid phase was present under high pressure (P) and temperature (T). In BSE-images, liquids are identified by a dendritic habitus which is typical for quenched carbonate melts (Vernon 2004). In contrast, carbonates crystallized during the experiment are coarser grained and have sharp, regular crystal forms. Throughout the text, the terms ‘melt’ and ‘solid’ will refer to the state of the matter under high PT. Solid carbonates are magnesite crystals in experiments using CM1. In experiments using CM2, Raman spectroscopy implies Mg-bearing calcite as solid carbonate, but disordered carbonate could also appear (Buob et al. 2006).

Carbonate crystals and carbonate melt are spatially separated in run A, B and C, whereby melt occurs in pools centered in the middle of the Pt-capsule and solids occur on both ends of the capsule in a semicircle reminding on an hourglass (Figure 1a, b, c). In run D, melt occurs interstitial between magnesite crystals with a diameter $\lesssim$10 µm (Figure 1d, h). Calcite crystals are larger grained with diameters up to $\lesssim$0.5 mm and show cleavage planes (run A, run B). In run A, small amounts of periclase crystals occur within melt pools and surrounded by calcite grains at the rims of the capsule (Figure 1e). Degassing of the melt upon quenching may have triggered the formation of periclase, or small amounts of periclase were present as inclusions in the natural magnesite used in the starting mixtures.

For each experiment, the proportions of the solid and liquid phase were constrained from geometric observations and using computed densities of solid carbonates (for details on the mass-balance calculations the reader is referred to the Methods section). The phase

proportions depend on the bulk composition and increase with temperature (Table 1). Using the obtained phase proportions (Table 1) and measured compositions, X_{Mg} of the bulk system was calculated and is consistent within a deviation of ~1.5% to ~5% to X_{Mg} of the starting mixtures. This demonstrates that the obtained proportions are reliable and implies equilibrium since the lever ruler is fulfilled.

Figure 1

Major element compositions

Ca-magnesite with X_{Mg}=0.89 (run D) and magnesite with X_{Mg}=0.96 (run C) are formed in experiments using starting mixture CM1 (Table 1). Note that, 'Ca-magnesite' and 'magnesite' will be used to refer to magnesite with X_{Mg}=0.89 and X_{Mg}=0.96, respectively. Using CM2 in run A and run B, calcite crystals with X_{Mg} of 0.14 and 0.19 are formed (Table 1). Within a single experiment, the major (and trace) element composition of carbonates is homogeneous and uniform across the capsule. Only in run B, two small ($\lesssim$50 μm) calcite grains at the bottom of the capsule with X_{Mg}=0.28 differ compositionally from the overall calcite composition (X_{Mg}=0.19).

To constrain the major and minor element composition of the melt, EPMA analyses were performed with a beam size of 20-40 μm, which exceeds the size of dendritic carbonate crystals (Figure 1e-g). The beam size was reduced to 1 μm to analyze the melt composition in run D (Figure 1h). All melts are dolomitic with X_{Mg} ranging between 0.5 to 0.8 for experiments performed with CM1 (run D, C) and between 0.31 to 0.33 for experiments performed with CM2 (run A, B; Table 1).

Table 1

Trace elements and partition coefficients

With LA-ICP-MS we determined the trace element composition of carbonates and melt except for run D where melt-pools are so small (Figure 1h) that several analyzes were

220 contaminated by neighbouring carbonate grains. Additionally to LA-ICP-MS, the
221 concentrations of Mn, Fe, Ba and Sr were determined by EPMA for all phases. The EPMA
222 results correlate well with concentrations obtained by LA-ICP-MS (Figure 2). Also, the trace
223 element concentration of the melt was constrained from mass-balance calculations. Hereby,
224 the trace element content in the melt is calculated from the known concentrations in the
225 starting materials, the measured concentrations in carbonates and using the proportions of
226 melt and carbonates listed in Table 1. The measured trace element content of the melt
227 corresponds, within the uncertainty, to the calculated concentrations (Figure 2). Thus, the
228 mass-balance approach is suitable to constrain the trace element concentration in run D.

229 **Figure 2**

230 Normalizing the trace element concentrations to the starting material demonstrates that Li,
231 Na, K, Nb and most REEs are enriched in the melt (Figure 3). The mass-balance approach
232 cannot be applied for elements forming alloys with the Pt of the capsule, because the bulk
233 amount is overestimated. Elements like Mn, Fe, Pb, Pr, Gd and Tb which are depleted in
234 carbonate grains and the melt of the same experiment, may have formed alloys with the Pt of
235 the capsule assuming the composition of the starting mixture is well defined.

236 **Figure 3**

237 Partition coefficients for Li, Na, K, Sr, Ba, Nb, Y and REEs (except Pr, Gd and Tb) between
238 magnesite, Ca-magnesite or calcite and dolomitic melt have been established. Assuming trace
239 elements *(i*) obey Henry's law, the partition coefficient (*D*) can be defined as quotient of the
240 concentration of an element in the solid-carbonate (c_i^s) and its concentration in the liquid
241 phase (c_i^l).

$$D_i^{s-l} = \frac{c_i^s}{c_i^l}$$

242 Sr and Ba are moderately incompatible in calcite with *D* ranging from 0.63±0.05 to 0.8±0.2
243 and from 0.14±0.05 to 0.26±0.07 (run A, B; Table 2). Single charged Li, Na and K are

incompatible in calcite with *D* ranging from 0.03 to 0.3 (Table 2). Trivalent Y and REEs are moderately incompatible in calcite with *D* between 0.2 and 0.3, whereby LREEs (La, Ce, Nd, Sm) are slightly less compatible compared to HREEs (Eu, Dy, Ho, Er, Tm, Yb, Lu, Y) (classification of REEs taken from the Geological-Society-London (2011)). Nb is incompatible in calcite with $D \lesssim 0.002$.

Li, Na and K are incompatible in magnesite and strongly enriched in the dolomitic melt. Partitioning coefficients of Sr, Ba, Y, REEs and Nb between Ca-magnesite (X_{Mg} =0.89) and dolomitic melt (X_{Mg}=0.5) at 1400 °C are between ~0.1 and 0.2 (run D; Table 2). The partition coefficients between magnesite (X_{Mg}=0.96) and dolomitic melt (X_{Mg}=0.8) at 1600 °C increase continuously from ~0.001 to ~0.1 between LREEs and HREEs (run C; Table 2). Similar, the compatibility of magnesite for Sr and Ba decreases with decreasing Ca content and increasing temperature (Table 2). For instance, the partition coefficient of Sr between Ca-magnesite (X_{Mg}=0.89) and dolomitic melt (X_{Mg}=0.5) is ~0.1 at 1400 °C (run D) but is reduced to 0.009±0.001 as Ca in magnesite decreases to X_{Mg}=0.96 at 1600 °C (run C).

Table 2

Discussion

By performing high PT-experiments, this study resolves the suprasolidus phase relations of Ca-Mg-carbonates at 6 GPa and determines trace element partition coefficients between calcite, Ca-magnesite or magnesite and dolomitic melt. In the discussion, first the approach to equilibrium will be considered. Then, the obtained suprasolidus phase relations will be compared to recent literature and thermodynamic modelling and, finally, the trace element partition coefficients will be discussed.

Approach to equilibrium

Multiple lines of evidence support equilibrium established during the experiment. The absence of compositional zoning in all experiments supports chemical equilibrium. In all experiments carbonates are homogeneous in their major and trace element composition as evidenced by EPMA and LA-ICP-MS profiles. Equilibrium is further supported by the applicability of the lever rule and by the good correlation of the liquidus between our experiments and the thermodynamic modelling (see next section and Figure 4b). The multi-anvil press was rotated throughout the entire run duration (stopping the rotation $\lesssim$30 sec before quenching) enhancing equilibrium between solids and a mobile phase (Schmidt and Ulmer 2004). Except for run D, liquid and solids are sequestrated after the experiment. Limited interconnectivity and the relative small melt proportion in run D may have hampered the spatial separation of the liquid and carbonate crystals. In run D melt-pockets occur in triple-junctions between homogenous Ca-magnesite crystals suggesting equilibrium (Hunter and McKenzie 1989). The 'hourglass' texture in run A, B and C, with solids in a semicircle on both ends of the capsule and the liquid phase in the middle, has previously been reported for fluid saturated systems (Deon et al. 2011). This hourglass texture might be due to a small thermal gradient with the hottest part in the centre of the capsule. Nonetheless, the absence of a temperature gradient has previously been verified for the same experimental set-up by applying the two-pyroxene system as an internal thermometer (see Figure 3 in Müller et al. (2017)). Adhesive and/or centrifugal forces may have fostered the development of the hourglass texture during rotation. In any case, Müller et al. (2017) demonstrated that a hydrous, CO_2-rich fluid and carbonates are intermingled when the experiment is quenched during rotation of the multi-anvil press (their Figures 6 a-c). Thus, they concluded that the mobile phase first separates from the solid phase when the rotation is stopped.

Suprasolidus phase relations

Suprasolidus phase relations depend on the bulk composition and are controlled either by the Ca-rich or Mg-rich part relative to the peritectic point (P1, Figure 4). Experimental studies constrained the peritectic point at 6 GPa to X_{Mg}~0.35-0.5 and 1300-1400 °C, but report an offset of up to ~120 °C for the liquidus temperature of Ca-rich carbonates and a larger discrepancy in temperature of up to ~200 °C for Mg-rich carbonates (Buob 2003; Buob et al. 2006; Müller et al. 2017; Shatskiy et al. 2018). This T-discrepancy is particularly crucial since it affects the onset and extent of melting assuming a mantle temperature of 1375-1490 °C at ~200 km (Ita and Stixrude 1992; McKenzie et al. 2005). For instance, at 1375 °C, Ca-Mg-carbonates may either be stable or may completely melt over a compositional range of $0.2 \lesssim X_{Mg} \lesssim 0.5$ (Müller et al. 2017; Shatskiy et al. 2018). Because of this discrepancy in the suprasolidus phase relations, key experiments were performed unravelling that carbonates will melt at 6 GPa for temperatures above ~1300 °C.

Melting was evidenced in all experiments by the presence of a liquid and crystalline phase. The median composition of solid carbonates and carbonate melt is plotted in Figure 4 and the error represents the complete analytical range (minimum to maximum) without outlier rejection. In comparison to previous, experimental studies by Müller et al. (2017) and Shatskiy et al. (2018), the here reported suprasolidus phase relations are complementary for compositions Ca-richer to the peritectic point and intermediate for Mg-richer compositions (Figure 4a). Buob (2003) and Buob et al. (2006) are not considered for a direct comparison, because they report quench problems and thus extrapolated the liquidus curve for the Mg-rich side based on two experiments performed below 1400 °C. Differences in the experimental results could be caused by a T-gradient in the capsule and the hydroscopic nature of the starting materials. Further, redox conditions and errors in quantification of the composition of run products may contribute to the different results. A T-gradient is unavoidable in high PT

316 experiments, but can be reduced by using a stepped graphite heater (Walter et al. 1995), as
317 employed in this study. Using the same experimental set-up, a homogenous temperature
318 distribution, within ±1% at 6 GPa and 1500 °C, was verified utilizing the two pyroxene
319 thermometer (Müller et al. 2017). The presence of even small amounts of water likely
320 reduces the solidus. Buob (2003), Buob et al. (2006), Müller et al. (2017), Shatskiy et al.
321 (2018) and this study, all used ground carbonates in the starting mixes, which are hygroscopic
322 and thus may adsorb some water from the atmosphere. Care was taken to minimize addition
323 of water by storing the starting mixtures above 100 °C. Müller et al. (2017) reported the
324 formation of minor amounts of brucite in their experiments indicating the presence of some
325 water. This may contribute to the tentatively lower liquidus reported by Müller et al. (2017).
326 Here, Raman spectroscopy verified the absence of hydrous phases in all run products.
327 Furthermore, impurities can reduce the melting point. The total content of trace elements in
328 the starting mixtures was <1 wt%. Thus, a quasi-ideal behavior and consequently minor
329 affect on the phase relations is assumed. Redox conditions may affect phase relations and
330 carbonate melting (Foley 2011). Although redox conditions were not controlled, the choice of
331 graphite as heater in combination with Pt-capsules (this study and Müller et al. (2017)) and
332 graphite as capsule material (Shatskiy et al. 2018) might have established redox conditions
333 close to the CCO buffer.
334 Our experimentally obtained liquidus is confirmed by thermodynamic modelling of the
335 $CaCO_3$-$MgCO_3$ system (Figure 4b). The computed and experimentally obtained compositions
336 of solid carbonates and carbonate melt correlate within a derivation of <8% for Mg-rich bulk
337 compositions (Table 1). Modeled, subsolidus phase relation for Ca-rich compositions might
338 be affected by the reaction of aragonite and magnesite to dolomite for temperatures ≳1000 °C
339 at 6 GPa (Buob et al. 2006; Franzolin et al. 2011). This reaction is not considered in the
340 thermodynamic modeling, because the used solid solution model for carbonates from

Franzolin et al. (2011) was calibrated based on experiments performed at pressures ≤3.5 GPa. Consequently, the model may misleadingly predict aragonite at ~1300-1500 °C, whereby aragonite was not observed at 6 GPa.

Figure 4

Trace element partitioning

Ca-Mg-carbonates can contain variable amounts of Li, K, Na, Mn, Fe, Ba, Sr, Pb and REEs (Dawson and Hinton 2003; Ionov and Harmer 2002; Ionov et al. 1996). Partial melting of carbonates will enrich some trace elements in the melt. Complementary, crystallization of carbonates from a CO_2-rich melt will sequester trace elements compatible in newly formed carbonates. Thus, the partition coefficients between calcite and dolomitic melt at 1350-1442 °C (Figure 5a), magnesite and dolomitic melt at 1600 °C (Figure 5b) and Ca-magnesite and dolomitic melt at 1400 °C (Figure 5b) were established at 6 GPa. The investigated range in bulk X_{Mg} and temperature enables to discuss the incorporation of trace elements in context of different X_{Mg}, temperature and carbonate structure ($R\bar{3}c$ for magnesite versus $R\bar{3}m$ for calcite at the investigated PT-conditions; Fiquet et al. (1994); Ishizawa (2014)). In the presence of magnesite, single charged cations are strongly enriched in the melt and the concentrations of Li, Na and K in magnesite are below the LA-ICP-MS detection limits (Table 2). Calcite, in contrast, can incorporate to some extent single charged cations and Na^+, with an ionic radii similar to Ca^{2+}, is with D ~ 0.1 - 0.3 slightly more compatible than Li+ ($0.03 \leq D \leq 0.07$) and K^+ ($0.1 \leq D \leq 0.24$) (Figure S1a and S1b in the supplementary information). Also, the partition coefficients of divalent cations between calcite and dolomitic melt increase in a parabolic trend as their size of the cations approaches the radius of Ca^{2+} (Figure S1a-b). For instance, the partition coefficient between calcite and dolomitic melt (run A and B) decreases from Sr^{2+} to Ba^{2+} (Table 2, Figure S1a-b). Therefore, the partitioning of divalent cations into calcite seems to follow lattice constraints (as employed by Blundy

366 and Wood (2003); Goldschmidt (1937)). Also, the distribution of divalent cations into
367 magnesite seems to follow lattice constraints: the larger the difference between the radii of a
368 particular cation to the size of Mg^{2+}, the lower the partition coefficient between magnesite
369 and dolomitic melt and thus $D(Sr^{2+}) > D(Ba^{2+})$ (Figure S1c-d). Increasing Ca-content in
370 magnesite and decreasing temperature enhance the incorporation of cations with a radius
371 similar or larger to Ca^{2+} like Ba^{2+}, Sr^{2+} and $LREEs^{3+}$ (Figure S1c-d). For instance, partition
372 coefficients of Sr and Ba between Ca-magnesite (X_{Mg}=0.89) and dolomitic melt (X_{Mg}=0.5) at
373 1400 °C (run D) are ~10 to ~1000 times larger than between magnesite (X_{Mg}=0.96) and
374 dolomitic melt (X_{Mg}=0.8) at 1600 °C (run C). Also LREEs become more compatible as the
375 Ca-content in magnesite increase (and temperature decreases). The partition coefficients of Y
376 and REEs between magnesite (X_{Mg}=0.96) and dolomitic melt (X_{Mg}=0.8) range from ~0.001 to
377 0.1 for LREEs to HREEs at 1600 °C (run C). In contrast, partition coefficients of REEs, Sr,
378 Ba, Nb and Y between Ca-richer magnesite ($X_{Mg=}$0.89) and dolomitic melt (X_{Mg}~0.5) are
379 more uniform scattering marginal between 0.1 and 0.2 at ~1400 °C (run D) (Figure 5b).

380 **Figure 5**

381 ## Implications

382 This study shows that Ca-Mg-carbonates with X_{Mg} ranging from 0.2 to 0.85 will (partially)
383 melt at 6 GPa and temperatures above ~1300 °C producing a dolomitic melt. Consequently,
384 CO_2 will be liberated by partial melting of an upwelling carbonated mantle at a depth of
385 ~200 km considering the thermal structure of the upper mantle (Ita and Stixrude 1992;
386 McKenzie et al. 2005). The results also affirm that, in the absence of water, carbonates will
387 be stable in the subducting slab even for hot subduction zone geotherms (Syracuse et al.
388 2010).

389 Low-degree melting of carbonated peridotite and carbonated eclogite in the mantle produces
390 a CO_2-rich liquid (Brey et al. 2008; Dalton and Presnall 1998; Dasgupta and Hirschmann

2006; Dasgupta et al. 2004; Foley et al. 2009; Yaxley and Green 1994; Yaxley and Brey 2004). The onset and composition of the incipient melt is influenced by the melt relations of the $CaCO_3$-$MgCO_3$-system, as comparisons between the pure carbonate and carbonated, low-alkali silicate systems have shown (Buob 2003; Buob et al. 2006; Shatskiy et al. 2018). This similarity suggests that decisive information like melting temperature and composition obtained from the pure Ca-Mg-carbonate system can be extrapolated, to some extent, to chemically more complex systems (containing Si, Al and minor amounts of K and Na) like carbonated peridotites and carbonated eclogites. This similarity in the major element composition (X_{Mg}) of a melt produced in the pure $CaCO_3$-$MgCO_3$-system versus a melt produced by low-degree melting of a carbonated, low-alkali silicates raises the question, to which extent also the trace element signature of the incipient melt is influenced by the pure carbonate system. Green et al. (1992) reported partition coefficients for a sodic, dolomitic carbonatite magma coexisting with a pargasite-augite-garnet-carbonate assemblage at 2.5 GPa and 1000 °C. X_{Mg} of the carbonatite magma and carbonate crystals is ~0.46 and ~0.43, respectively (Green et al. 1992; Wallace and Green 1988). Although carbonates (X_{Mg}=0.14-0.19) and dolomitic melt (X_{Mg}~0.3) in experiments performed with CM2 are Ca-richer, the partition coefficients for REEs and Sr correlate well (Figure 5a). This observation implies that the REEs and Sr signature of incipient melts of a SiO_2-bearing carbonated system can be approximated by the pure carbonate system.

Increasing Ca-content and decreasing temperature enhance the compatibility of Sr, Ba and LREEs into magnesite (Figure 5b). The compatibility of magnesite for Y and REEs seems further to be affected by the mineral assemblage. For instance, Dasgupta et al. (2009) reported partition coefficients between a magnesite-garnet-lherzolithe assemblage and carbonatitic melt at 6.6 GPa and 1265-1300 °C. X_{Mg} of magnesite (0.9±0.03) and dolomitic melt (0.41±0.05) from the experimental study of Dasgupta et al. (2009) are approximated by

run D performed at similar PT-conditions (6 GPa and 1400 °C). Nevertheless, the trace element distribution into magnesite differs (Figure 5b). A carbonatitic melt in equilibrium with a magnesite-garnet-lherzolithe likely shows an enrichment of LREEs over HREEs, whereby in the $CaCO_3$-$MgCO_3$-system such fractionation would only be expected for melting at higher temperature (1600 °C) (run C; Figure 5b).

Conclusions

The suprasolidus phase relations of the nominally anhydrous $CaCO_3$-$MgCO_3$-system at 6 GPa were studied by performing multi-anvil experiments. The results demonstrate that:

- (partial) melting of Ca-Mg-carbonates occurs at 6 GPa for temperatures above ~1300 °C. Consequently, carbonates are stable during subduction even for hot subduction zone geotherms (Syracuse et al. 2010) unless carbonate bearing lithologies in the slab are infiltrated by aqueous fluids. Considering the thermal structure of the mantle (Ita and Stixrude 1992; McKenzie et al. 2005), CO_2 will be released by (partial) melting of carbonates during upwelling of a carbonated mantle.
- In calcite (X_{Mg}=0.14-0.19), Li, Na, K, Sr, Ba, Y and REEs are slightly incompatible with partition coefficients around ~0.1-0.8. Trace element distribution between calcite and dolomitic melt seems to follow lattice constraints for divalent cations.

  In magnesite (X_{Mg}=0.89-0.96), Sr, Ba, Y and REEs become more compatible with increasing Ca-content and decreasing temperature. Partition coefficients of Y and REEs between magnesite (X_{Mg}=0.96) and dolomitic melt (X_{Mg}=0.8) range from ~0.001 to 0.1 for LREEs to HREEs at 1600 °C. In comparison, partition coefficients of REEs, Sr, Ba, Nb and Y between Ca-magnesite (X_{Mg}=0.89) and dolomitic melt (X_{Mg}=0.5) are more uniform scattering marginal between ~0.1 and 0.2 at ~1400 °C.

Acknowledgments

We are grateful to A. Ebert, O. Appelt and C. Wohlgemuth-Überwasser for their assistance in experimental and analytical work. We like to thank A. Shatskiy and an anonymous reviewer for their constructive comments and C. E. Lesher for editorial handling of the paper. This study was funded by the DFG funded research group FOR2125 CarboPaT under the grant number KO1260/19-1.

References

Alt, J. C., and Teagle, D. A. (1999) The uptake of carbon during alteration of ocean crust. Geochimica et Cosmochimica Acta, 63, 1527-1535.

Blundy, J., and Wood, B. (2003) Partitioning of trace elements between crystals and melts. Earth and Planetary Science Letters, 210, 383-397.

Brey, G. P., Bulatov, V. K., Girnis, A. V., and Lahaye, Y. (2008) Experimental melting of carbonated peridotite at 6-10 GPa. Journal of Petrology, 49, 797-821.

Buob, A. (2003) The System CaCO3-MgCO3: Experiments and Thermodynamic Modeling of the Trigonal and Orthorhombic Solid Solutions at High Pressure and Temperature: PhD thesis.

Buob, A., Schmidt, M. W., Ulmer, P., and Luth, R. W. (2006) Experiments on CaCO3-MgCO3 solid solutions at high pressure and temperature. American Mineralogist, 91, 435-440.

Connolly, J. A. D. (2005) Computation of phase equilibria by linear programming: A tool for geodynamic modeling and its application to subduction zone decarbonation. Earth and Planetary Science Letters, 236, 524-541.

Dalton, J. A., and Wood, B. J. (1993) The compositions of primary carbonate melts and their evolution through wallrock reaction in the mantle. Earth and Planetary Science Letters, 119, 511-525.

Dalton, J. A., and Presnall, D. C. (1998) The Continuum of Primary Carbonatitic–Kimberlitic Melt Compositions in Equilibrium with Lherzolite: Data from the System CaO–MgO–Al2O3–SiO2–CO2 at 6 GPa. Journal of Petrology, 39, 1953-1964.

Dasgupta, R., and Hirschmann, M. M. (2006) Melting in the Earth's deep upper mantle caused by carbon dioxide. Nature, 440, 659.

Dasgupta, R., and Hirschmann, M. M. (2010) The deep carbon cycle and melting in Earth's interior. Earth and Planetary Science Letters, 298, 1-13.

Dasgupta, R., Hirschmann, M. M., and Withers, A. C. (2004) Deep global cycling of carbon constrained by the solidus of anhydrous, carbonated eclogite under upper mantle conditions. Earth and Planetary Science Letters, 227, 73-85.

Dasgupta, R., Hirschmann, M. M., McDonough, W. F., Spiegelman, M., and Withers, A. C. (2009) Trace element partitioning between garnet lherzolite and carbonatite at 6.6 and 8.6 GPa with applications to the geochemistry of the mantle and of mantle-derived melts. Chemical Geology, 262, 57-77.

Dawson, J., and Hinton, R. (2003) Trace-element content and partitioning in calcite, dolomite and apatite in carbonatite, Phalaborwa, South Africa. Mineralogical Magazine, 67, 921-930.

Deon, F., Koch-Müller, M., Rhede, D., and Wirth, R. (2011) Water and Iron effect on the P-T-x coordinates of the 410-km discontinuity in the Earth upper mantle. Contributions to Mineralogy and Petrology, 161, 653-666.

Fiquet, G., Guyot, F., and Itie, J.-P. (1994) High-pressure X-ray diffraction study of carbonates: MgCo3, CaMg(CO3)2, and CaCO3. American Mineralogist, 79, 15-23.

Foley, S. F. (2011) A Reappraisal of Redox Melting in the Earth's Mantle as a Function of Tectonic Setting and Time. Journal of Petrology, 52, 1363-1391.

Foley, S. F., Yaxley, G. M., Rosenthal, A., Buhre, S., Kiseeva, E. S., Rapp, R. P., and Jacob, D. E. (2009) The composition of near-solidus melts of peridotite in the presence of CO2 and H2O between 40 and 60 kbar. Lithos, 112, 274-283.

Franzolin, E., Schmidt, M. W., and Poli, S. (2011) Ternary Ca–Fe–Mg carbonates: subsolidus phase relations at 3.5 GPa and a thermodynamic solid solution model including order/disorder. Contributions to Mineralogy and Petrology, 161, 213-227.

Gaillard, F., Malki, M., Iacono-Marziano, G., Pichavant, M., and Scaillet, B. J. S. (2008) Carbonatite melts and electrical conductivity in the asthenosphere, 322, 1363-1365.

Geological-Society-London, 2011: Rare Earth Elements A briefing note by the Geological Society of London. December 2011 ed.

Goldschmidt, V. M. (1937) The principles of distribution of chemical elements in minerals and rocks. The seventh Hugo Müller Lecture, delivered before the Chemical Society on March 17th, 1937. Journal of the Chemical Society (Resumed), 655-673.

Gorman, P. J., Kerrick, D. M., and Connolly, J. A. D. (2006) Modeling open system metamorphic decarbonation of subducting slabs. Geochemistry, Geophysics, Geosystems, 7, n/a-n/a.

Green, T. H., Adam, J., and Siel, S. H. (1992) Trace element partitioning between silicate minerals and carbonatite at 25 kbar and application to mantle metasomatism. Mineralogy and Petrology, 46, 179-184.
Hazen, R. M., Jones, A. P., and Baross, J. A., 2013: Carbon in earth. Vol. 75.
Hirschmann, M. M. (2000) Mantle solidus: Experimental constraints and the effects of peridotite composition. Geochemistry, Geophysics, Geosystems, 1.
Holland, T. J. B., and Powell, R. (1998) An internally consistent thermodynamic data set for phases of petrological interest. Journal of Metamorphic Geology, 16, 309-343.
Hunter, R. H., and McKenzie, D. (1989) The equilibrium geometry of carbonate melts in rocks of mantle composition. Earth and Planetary Science Letters, 92, 347-356.
Ionov, D., and Harmer, R. E. (2002) Trace element distribution in calcite–dolomite carbonatites from Spitskop: inferences for differentiation of carbonatite magmas and the origin of carbonates in mantle xenoliths. Earth and Planetary Science Letters, 198, 495-510.
Ionov, D. A., Dupuy, C., O'Reilly, S. Y., Kopylova, M. G., and Genshaft, Y. S. (1993) Carbonated peridotite xenoliths from Spitsbergen: implications for trace element signature of mantle carbonate metasomatism. Earth and Planetary Science Letters, 119, 283-297.
Ionov, D. A., O'Reilly, S. Y., Genshaft, Y. S., Kopylova, M. G. J. C. t. M., and Petrology (1996) Carbonate-bearing mantle peridotite xenoliths from Spitsbergen: phase relationships, mineral compositions and trace-element residence, 125, 375-392.
Ishizawa, N. (2014) Calcite V: a hundred-year-old mystery has been solved. Powder Diffraction, 29, S19-S23.
Ita, J., and Stixrude, L. (1992) Petrology, elasticity, and composition of the mantle transition zone. Journal of Geophysical Research: Solid Earth, 97, 6849-6866.
Jochum, K. P., Weis, U., Stoll, B., Kuzmin, D., Yang, Q., Raczek, I., Jacob, D. E., Stracke, A., Birbaum, K., Frick, D. A., Günther, D., and Enzweiler, J. (2011) Determination of Reference Values for NIST SRM 610–617 Glasses Following ISO Guidelines. Geostandards and Geoanalytical Research, 35, 397-429.
Kelemen, P. B., and Manning, C. E. (2015) Reevaluating carbon fluxes in subduction zones, what goes down, mostly comes up. Proceedings of the Natlional Academy of Sciences USA, 112, E3997-4006.
Keppler, H. (2003) Water solubility in carbonatite melts. American Mineralogist, 88, 1822-1824.
Kerrick, D. M., and Connolly, J. A. D. (1998) Subduction of ophicarbonates and recycling of CO2 and H2O. Geology, 26, 375-378.
Kerrick, D. M., and Connolly, J. A. D. (2001) Metamorphic devolatilization of subducted oceanic metabasalts: implications for seismicity, arc magmatism and volatile recycling. Earth and Planetary Science Letters, 189, 19-29.
Korsakov, A. V., and Hermann, J. (2006) Silicate and carbonate melt inclusions associated with diamonds in deeply subducted carbonate rocks. Earth and Planetary Science Letters, 241, 104-118.
Kruk, A. N., Sokol, A. G., and Palyanov, Y. N. J. P. (2018) Phase Relations in the Harzburgite–Hydrous Carbonate Melt at 5.5–7.5 GPa and 1200–1350°C, 26, 575-587.
McKenzie, D., Jackson, J., and Priestley, K. (2005) Thermal structure of oceanic and continental lithosphere. Earth and Planetary Science Letters, 233, 337-349.
Müller, J., Koch-Müller, M., Rhede, D., Wilke, F. D., and Wirth, R. (2017) Melting relations in the system CaCO3-MgCO3 at 6 GPa. American Mineralogist: Journal of Earth and Planetary Materials, 102, 2440-2449.
Piccoli, F., Vitale Brovarone, A., Beyssac, O., Martinez, I., Ague, J. J., and Chaduteau, C. (2016) Carbonation by fluid–rock interactions at high-pressure conditions: Implications for carbon cycling in subduction zones. Earth and Planetary Science Letters, 445, 146-159.
Scambelluri, M., Bebout, G. E., Belmonte, D., Gilio, M., Campomenosi, N., Collins, N., and Crispini, L. (2016) Carbonation of subduction-zone serpentinite (high-pressure ophicarbonate; Ligurian Western Alps) and implications for the deep carbon cycling. Earth and Planetary Science Letters, 441, 155-166.
Schmidt, M. W., and Ulmer, P. (2004) A rocking multianvil: elimination of chemical segregation in fluid-saturated high-pressure experiments. Geochimica et Cosmochimica Acta, 68, 1889-1899.
Shannon, R., and Prewitt, C. (1970) Revised values of effective ionic radii. Acta Crystallographica Section B: Structural Crystallography and Crystal Chemistry, 26, 1046-1048.
Shannon, R. T., and Prewitt, C. T. (1969) Effective ionic radii in oxides and fluorides. Acta Crystallographica Section B: Structural Crystallography and Crystal Chemistry, 25, 925-946.
Shatskiy, A., Podborodnikov, I. V., Arefiev, A. V., Minin, D. A., Chanyshev, A. D., and Litasov, K. D. (2018) Revision of the CaCO3–MgCO3 phase diagram at 3 and 6 GPa. American Mineralogist, 103, 441-452.
Shatsky, V., Ragozin, A., and Sobolev, N. (2006) Some aspects of metamorphic evolution of ultrahigh-pressure calc-silicate rocks of the Kokchetav Massif. Russian Geology and Geophysics (Geologiya i Geofizika), 47, 105-119.
Sieber, M. J., Hermann, J., and Yaxley, G. M. (2018) An experimental investigation of C-O-H fluid-driven carbonation of serpentinites under forearc conditions. Earth and Planetary Science Letters, 496, 177-188.
Stachel, T., and Harris, J. W. (2008) The origin of cratonic diamonds — Constraints from mineral inclusions. Ore Geology Reviews, 34, 5-32.
Syracuse, E. M., van Keken, P. E., and Abers, G. A. (2010) The global range of subduction zone thermal models. Physics of the Earth and Planetary Interiors, 183, 73-90.
Vernon, R. H., 2004: A Practical Guide to Rock Microstructure. 2 ed. Vol. 1, Cambridge University Press.
Wallace, M. E., and Green, D. H. (1988) An experimental determination of primary carbonatite magma composition. Nature, 335, 343-346.
Walter, M. J., Thibault, Y., Wei, K., and Luth, R. W. (1995) Characterizing experimental pressure and temperature conditions in multi-anvil apparatus. Canadian Journal of Physics, 73, 273-286.
Wang, A., Pasteris, J. D., Meyer, H. O. A., and Dele-Duboi, M. L. (1996) Magnesite-bearing inclusion assemblage in natural diamond. Earth and Planetary Science Letters, 141, 293-306.

Watenphul, A., Wunder, B., and Heinrich, W. (2009) High-pressure ammonium-bearing silicates: Implications for nitrogen and hydrogen storage in the Earth's mantle. American Mineralogist, 94, 283-292.
Yaxley, G. M., and Green, D. H. (1994) Experimental demonstration of refractory carbonate-bearing eclogite and siliceous melt in the subduction regime. Earth and Planetary Science Letters, 128, 313-325.
Yaxley, G. M., and Brey, G. P. (2004) Phase relations of carbonate-bearing eclogite assemblages from 2.5 to 5.5 GPa: implications for petrogenesis of carbonatites. Contributions to Mineralogy and Petrology, 146, 606-619.
Zhang, X., Yang, S.-Y., Zhao, H., Jiang, S.-Y., Zhang, R.-X., and Xiae, J. (2017) Effect of beam current and diamter on electron probe microanalysis of carbonate minerals. Journal of Earth Science.

Tables caption

Table 1: Overview of the performed experiments. Two starting mixtures (CM1 and CM2) with a bulk X_{Mg} of 0.85 and 0.2 were used. In all experiments, liquid and solid carbonate phase were present under high pressures (6 GPa) and temperatures (T). Calculations of phase proportions are based on geometric constraints (e.g. observations from BSE-images) and computed densities of solid carbonates (see text for more details).

Table 2: Trace element concentration of carbonate crystals and carbonate melt and partition coefficient (*D*). The trace element composition of the melt in run D is calculated per mass-balance. All other concentrations are determined by LA-ICP-MS.

Figure caption

Figure 1: BSE-images of recovered capsules: (a, e) run A; (b, f) run B; (c, g) run C; (d, h) run D. In all experiments, a carbonate melt (liq) and solid carbonates (carb) are present. In run A small amounts of periclase (per) were observed.

Figure 2: The Sr (left) and Ba (right) composition of solid carbonates and carbonate melt were measured by EPMA-WDS (abscissa). The microprobe results correlate well with LA-ICP-MS measurements (ordinate) of carbonate crystals (diamonds) and melts (dark-gray circles). Mass-balance calculations (ordinate) also constrained the trace element compositions of the melts (light-gray circles). Within the uncertainties, the measured and calculated

590 compositions correlate well testifying the applicability of the mass-balance approach to
591 calculate the trace element composition of the melt.
592
593 Figure 3: Trace element compositions of carbonate crystals (white symbols) and carbonate
594 melts (red symbols) per LA-ICP-MS normalized to the start mixtures (CM1 and CM2).
595 LILEs, Nb, Y and REEs are enriched in the melts. Relative to the start mixtures, Fe, Mn, Pb,
596 Pr, Gd and Tb are depleted in carbonate crystals and carbonate melts indicating alloy
597 formation with the Pt capsule.
598
599 Figure 4: The here observed suprasolidus phase relations of the $CaCO_3$-$MgCO_3$-system at
600 6 GPa (black, thick curves and black, bold labels) are compared to (a) the experimental
601 studies of Shatskiy et al. (2018) (green, thin curves and green, italic labels) and Müller et al.
602 (2017) (blue, thin curves). In (b) our results are compared to thermodynamical modelled
603 phase relations (orange, thin curves and orange, italic labels). The model may misleadingly
604 predict aragonite at ~1300-1500 °C, because the reaction of aragonite and magnesite to
605 dolomite is not considered in the solid solution model (details in text). The median
606 composition of carbonate melts (gray circles) and carbonate crystals (open diamonds) per
607 WDS is plotted and the error bars represents the data range without outlier rejection.
608
609 Figure 5: Partition coefficients (D) between (a) calcite and dolomitic melt (run A and B) and
610 (b) magnesite and dolomitic melt (run C and D). The legend lists the starting mixtures (CM1,
611 CM2), the temperature [°C] and X_{Mg} of solid carbonates and melts.

612 **Supplementary**

613 Figure S1: Partition coefficient (D) as a function of charge and ionic radius for (a) run A, (b)
614 run B, (c) run C and (d) run D. Straight, solid lines refer to the 6-fold coordinated ionic radii

615 of Mg^{2+} (0.072 nm) and Ca^{2+} (0.1 nm) (Shannon and Prewitt 1970; Shannon and Prewitt
616 1969).

This is a preprint, the final version is subject to change, of the American Mineralogist (MSA)
Cite as Authors (Year) Title. American Mineralogist, in press.
DOI: https://doi.org/10.2138/am-2020-7098

experimental conditions				**observed phase**	calculated proportion	composition per FE-EPMA			per thermodynamic modelling			
run	T [°C]	start-mix	bulk X_{Mg}		[wt%]	X_{Mg} min	X_{Mg} average	X_{Mg} max	modelled phase	density [g/cm^3]	proportion [wt%]	X_{Mg}
A	1442	CM2	0.2	**melt**	32	0.29	0.31	0.32	melt		64	0.31
				calcite	68	0.10	0.14	0.17	aragonite	2.88	36	0.0
				periclase	uc						\	
B	1350	CM2	0.2	**melt**	6	0.30	0.33	0.36	melt		21	0.37
				calcite	94	0.17	0.19	0.21	carbonate	2.84	79	0.15
				calcite II	uc	0.20	0.28	0.32			\	
C	1600	CM1	0.85	**melt**	92	0.78	0.80	0.82	melt		95	0.84
				magnesite	8	0.96	0.96	0.97	carbonate	2.96	5	0.999
D	1400	CM1	0.85	**melt**	14	0.38	0.50	0.61	melt		26	0.53
				Ca-magnesite	86	0.87	0.89	0.91	carbonate	2.97	74	0.95

uc unconstrained

This is a preprint, the final version is subject to change, of the American Mineralogist (MSA)
Cite as Authors (Year) Title. American Mineralogist, in press.
DOI: https://doi.org/10.2138/am-2020-7098

	Run A (melt composition per LA-ICP-MS)			Run B (melt composition per LA-ICP-MS)			Run C (melt composition per LA-ICP-MS)			Run D (melt composition per LA-ICP-MS)			Run D (melt composition per mass balance)		
	calcite X_{Mg}=0.14 [ppm]	Melt X_{Mg}=0.31 [ppm]	D	calcite X_{Mg}=0.19 [ppm]	Melt X_{Mg}=0.33 [ppm]	D	magnesite X_{Mg}=0.96 [ppm]	Melt X_{Mg}=0.8 [ppm]	D	Ca-magnesite X_{Mg}=0.89 [ppm]	Melt X_{Mg}=0.5 [ppm]	D	Ca-magnesite X_{Mg}=0.89 [ppm]	Melt X_{Mg}=0.5 [ppm]	D
Li	2	51	0.03	5	77	0.07	<dl	30		<dl	179		<dl		
2σ	1	5	0.02	4	24	0.05		2			79				
Na	33	241	0.14	91	352	0.3	<dl	373		<dl	<dl		<dl		
2σ	20	36	0.08	46	105	0.2		48							
K	29	292	0.10	66	275	0.24	<dl	126		<dl	<dl		<dl		
2σ	10	38	0.04	10	86	0.08		15							
Mn	19	9		43	262		201	170		<dl	320		<dl		
2σ	15	1		8	32		10	7			135				
Fe	428	384		556	7069		260	175		<dl	995		<dl		
2σ	105	64		476	3434		15	32			645				
Sr	150	239	0.63	195	233	0.8	3	294	0.009	119	905	0.13	119	1481	0.10
2σ	12	6	0.05	40	11	0.2	0	7	0.001	53	138	0.06	53		
Y	117	344	0.3	119	427	0.28	13	319	0.042	126	658	0.19	126	1086	0.14
2σ	67	10	0.2	22	30	0.05	1	9	0.003	46	95	0.07	46		
Nb	0.3	537	0.0006	2.0	981	0.002	<dl	257		75	297	0.25	75	1351	0.07
2σ	0.2	36	0.0004	2.3	269	0.002		10		126	75	0.43	126		
Ba	90	664	0.14	165	634	0.26	0.0	418	0.0001	150	995	0.15	150	3164	0.06
2σ	30	25	0.05	27	140	0.07	0.8	24	0.0018	81	185	0.09	81		
La	132	745	0.2	153	909	0.17	0.7	528	0.0014	159	1305	0.12	159	1983	0.10
2σ	90	11	0.1	22	157	0.04	0.2	22	0.0004	59	210	0.05	59		
Ce	139	752	0.2	155	1195	0.13	1.4	537	0.0026	224	1755	0.13	224	1516	0.17
2σ	95	27	0.1	61	241	0.06	0.2	20	0.0004	95	290	0.06	95		
Pr	128	595		148	786		1.1	472		173	1375		173		
2σ	83	14		20	122		0.2	17		95	270		95		
Nd	167	631	0.3	175	790	0.22	2.1	502	0.004	180	1415	0.13	180	1946	0.11
2σ	108	35	0.2	39	86	0.06	0.5	26	0.001	85	260	0.06	85		
Sm	165	584	0.3	181	738	0.24	3.6	489	0.007	176	1205	0.15	176	2117	0.10
2σ	104	27	0.2	40	62	0.06	0.5	11	0.001	93	200	0.08	93		
Eu	193	524	0.4	213	759	0.28	5.2	505	0.010	174	1310	0.13	174	2163	0.10
2σ	81	15	0.2	66	64	0.09	0.6	16	0.001	83	235	0.07	83		
Gd	91	312		101	403		3.6	276		96	693		96		
2σ	55	10		18	38		0.7	7		43	130		43		
Tb	183	606		195	828		11.6	549		209	1335		209		
2σ	110	18		28	100		0.8	19		68	230		68		
Dy	187	615	0.3	209	849	0.25	15.8	536	0.029	199	1170	0.17	199	2220	0.11
2σ	112	19	0.2	32	89	0.05	1.1	12	0.002	55	190	0.05	55		
Ho	204	644	0.3	219	938	0.23	23.1	569	0.041	213	1200	0.18	213	2168	0.12
2σ	119	26	0.2	28	124	0.04	1.3	15	0.002	74	180	0.07	74		
Er	192	582	0.3	202	805	0.25	28.3	539	0.052	222	1115	0.20	222	2151	0.12
2σ	113	15	0.2	20	77	0.03	2.0	12	0.004	87	165	0.08	87		
Tm	215	681	0.3	228	998	0.23	36.4	525	0.069	243	1145	0.21	243	2031	0.14
2σ	121	36	0.2	32	97	0.04	2.2	13	0.005	89	145	0.08	89		
Yb	227	633	0.4	238	918	0.26	48.9	563	0.087	249	1150	0.22	249	2082	0.14
2σ	139	25	0.2	38	77	0.05	2.6	20	0.005	94	165	0.09	94		
Lu	196	581	0.3	225	850	0.26	56.0	497	0.113	239	945	0.25	239	2198	0.13
2σ	111	12	0.2	44	72	0.06	2.8	17	0.007	89	125	0.10	89		
Pb	31	5.3		317	169		0.7	34		7	68		7		
2σ	53	0.4		90	45		0.1	3		3	31		3		

<dl: below detection limit

This is a preprint, the final version is subject to change, of the American Mineralogist (MSA)
Cite as Authors (Year) Title. American Mineralogist, in press.
DOI: https://doi.org/10.2138/am-2020-7098

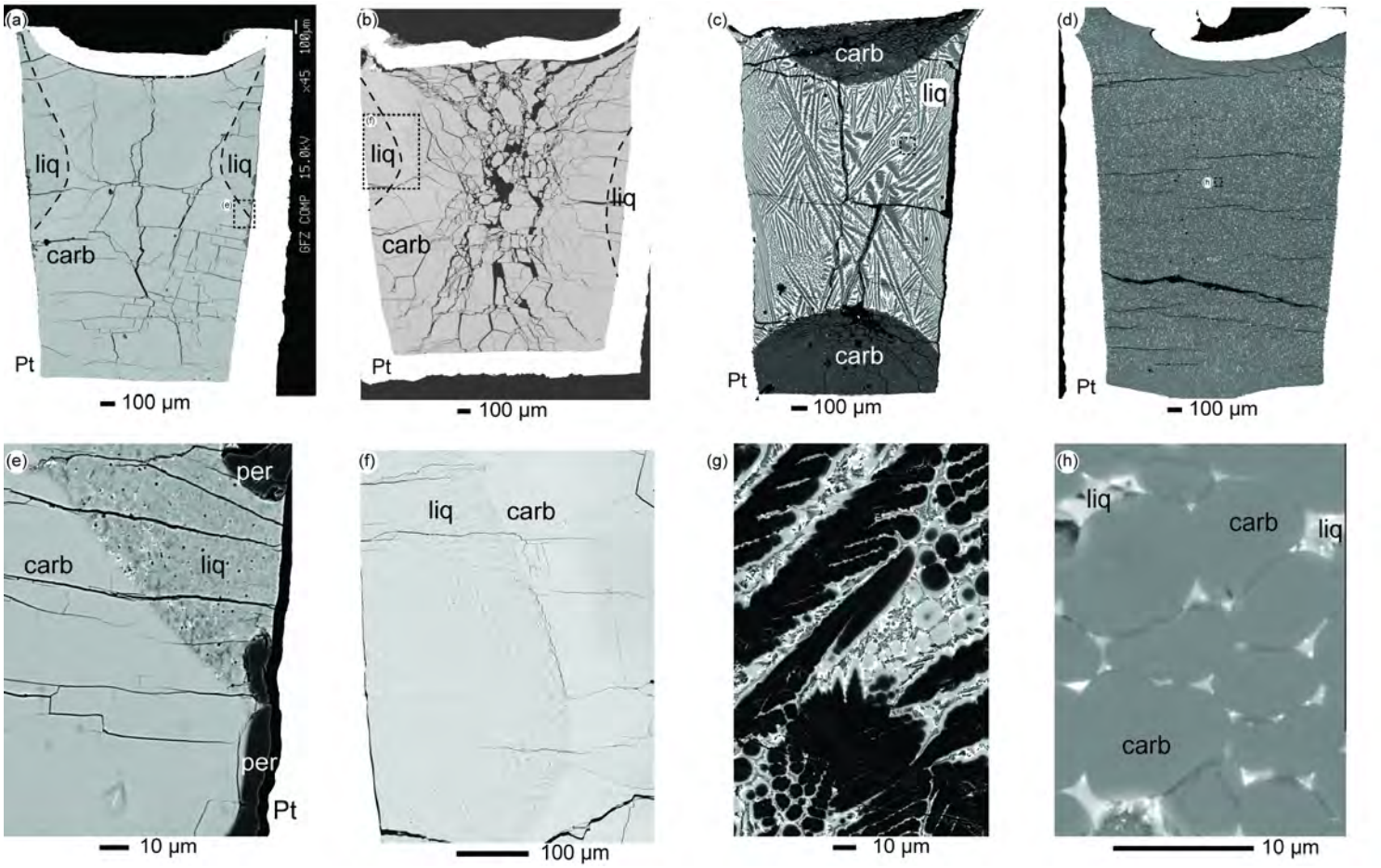

This is a preprint, the final version is subject to change, of the American Mineralogist (MSA)
Cite as Authors (Year) Title. American Mineralogist, in press.
DOI: https://doi.org/10.2138/am-2020-7098

Fig 2

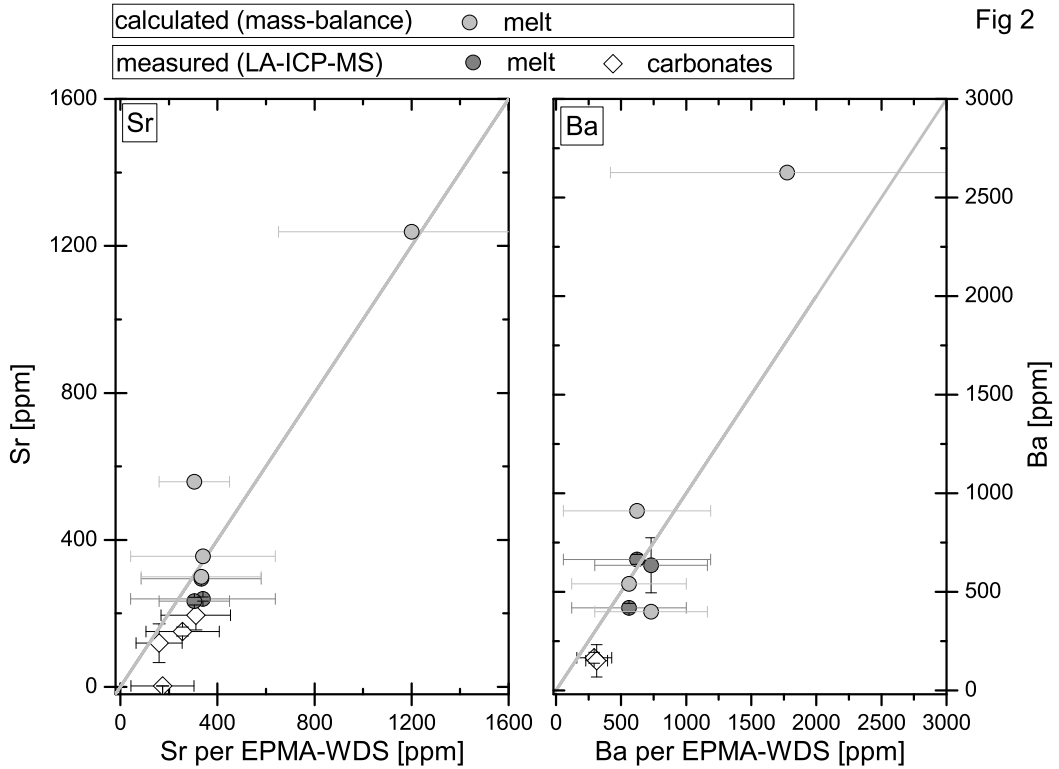

This is a preprint, the final version is subject to change, of the American Mineralogist (MSA)
Cite as Authors (Year) Title. American Mineralogist, in press.
DOI: https://doi.org/10.2138/am-2020-7098

Fig 3

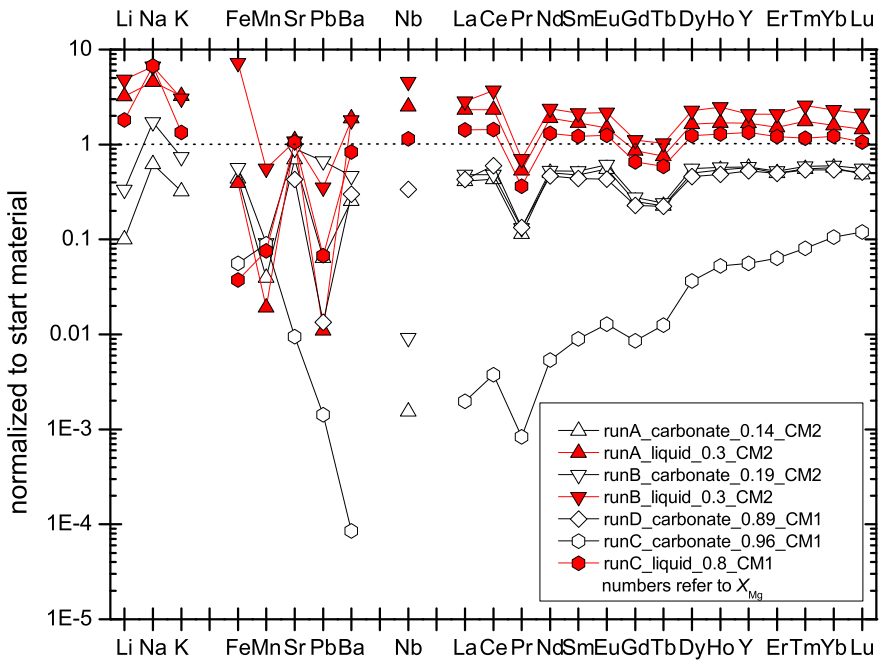

This is a preprint, the final version is subject to change, of the American Mineralogist (MSA)
Cite as Authors (Year) Title. American Mineralogist, in press.
DOI: https://doi.org/10.2138/am-2020-7098

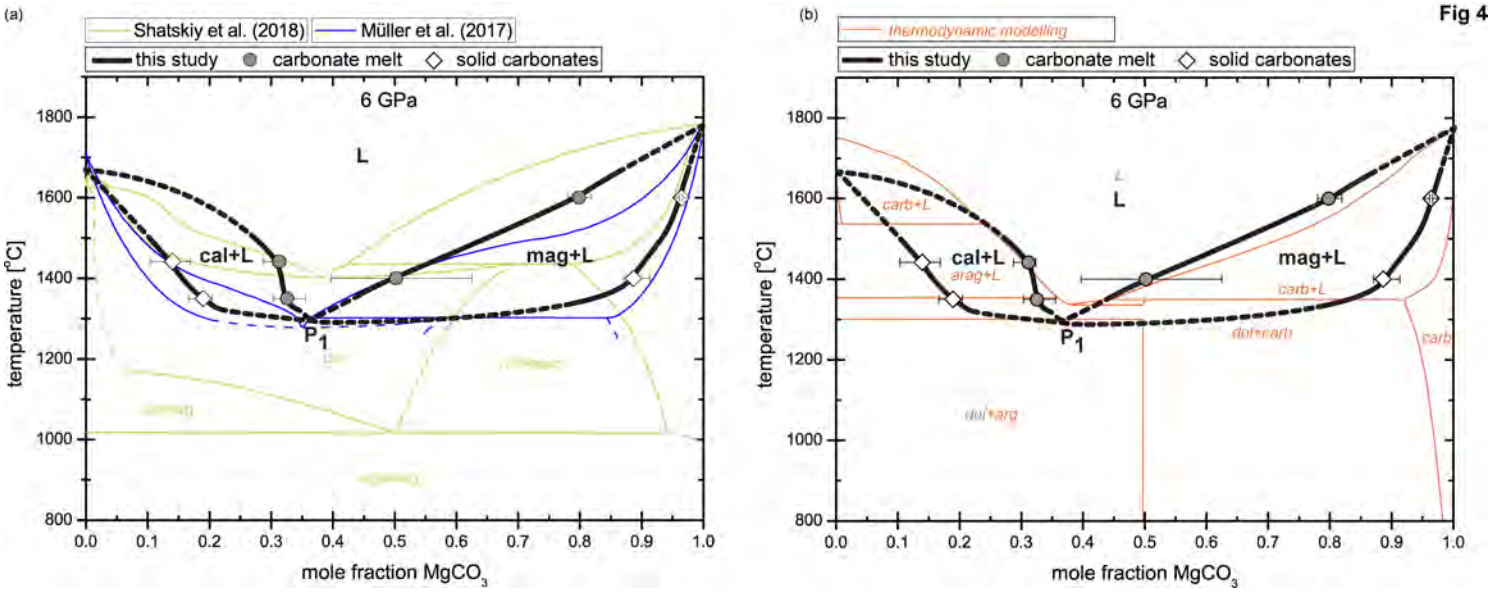

Fig 4

This is a preprint, the final version is subject to change, of the American Mineralogist (MSA)
Cite as Authors (Year) Title. American Mineralogist, in press.
DOI: https://doi.org/10.2138/am-2020-7098

Fig.5